

Theoretical description of optical and X-ray absorption spectra of MgO including many-body effects

Vijaya Begum,¹ Markus E. Gruner,¹ Christian Vorwerk,² Claudia Draxl,² and Rossitza Pentcheva¹

¹*Department of Physics and Center for Nanointegration Duisburg-Essen (CENIDE),*

University of Duisburg-Essen, Lotharstr. 1, 47057 Duisburg, Germany

²*Institute für Physik and IRIS Adlershof, Humboldt-Universität zu Berlin, Berlin, Germany
and European Theoretical Spectroscopy Facility*

(Dated: September 29, 2022)

Here we report the optical and x-ray absorption (XAS) spectra of the wide-band-gap oxide MgO using density functional theory (DFT) and many-body perturbation theory (MBPT). Our comprehensive study of the electronic structure shows that while the band gap is underestimated with the exchange-correlation functional PBEsol (4.58 eV) and the hybrid functional HSE06 (6.58 eV) compared to the experimental value (7.7 eV), it is significantly improved (7.52 eV) and even overcompensated (8.53 eV) when quasiparticle corrections are considered. Inclusion of excitonic effects by solving the Bethe-Salpeter equation (BSE) yields the optical spectrum in excellent agreement with experiment. Excellent agreement is observed also for the O and Mg K-edge absorption spectra, demonstrating the importance of the electron-hole interaction within MBPT. Projection of the electron-hole coupling coefficients from the BSE eigenvectors on the band structure allows us to determine the origin of prominent peaks and identify the orbital character of the relevant contributions. The real space projection of the lowest energy exciton wavefunction of the optical spectrum indicates a Wannier-Mott type, whereas the first exciton in the O K-edge is more localized.

I. INTRODUCTION

MgO is one of the most extensively studied oxides which is used as a substrate material and in various heterostructures with applications related to tunneling magnetoresistance [1–3]. Recently, this material was employed in transient x-ray spectroscopy and time-dependent density-functional theory (DFT) calculations aiming to unravel the propagation of excitations across the interface in metal-insulator heterostructures [4–7]. Understanding spectroscopic features from first-principles requires accurate modeling beyond the ground state properties including excitations of different origin and energy scale.

The structural and electronic properties of this wide band gap material with a measured band gap between 7.7 [8] and 7.83 eV [9] have been widely studied with first-principles calculations [10–12]. Unsurprisingly, DFT calculations with semilocal functionals significantly underestimate the band gap [10, 12, 13]. Many-body perturbation theory (MBPT) calculations employing Hedin’s GW approximation [14] yield an increased band gap [11, 12], which is still lower than the experimental one. The optical spectrum, calculated by Wang *et al.* [13] using the local density approximation (LDA) as the exchange-correlation functional for the DFT calculation and subsequently including GW and excitonic corrections agrees with experiment [15] w.r.t. peak positions up to 12 eV whereas the amplitude of the peaks beyond the first one is overestimated due to the limited number of unoccupied bands employed in the BSE corrections. Schleife *et al.* [10] studied the frequency-dependent dielectric function for different MgO polymorphs – wurzite, zinc blende, and rocksalt – in the independent particle (IP) approximation using the generalized gradient approximation in

the PW91 parametrization [16]. Good agreement with experiment concerning the peak positions was obtained by including excitonic corrections with BSE, based on the Kohn-Sham (KS) eigenenergies and a scissors operator to describe the QP eigenenergies [17, 18].

While optical spectroscopy probes excitations from valence bands, x-ray absorption spectroscopy (XAS) probes those from the strongly localized core states. A common approach to model XAS is the final state rule (FSR) [19] based on Fermi’s Golden rule, where the effects of screening of the core-hole (the so-called *final-state effects*) are calculated in a supercell. Alternatively, XAS can be described by considering quasiparticle and excitonic effects within MBPT by using GW and solving the BSE. Rehr *et al.* [20] showed that while both approaches led to similar overall features in the O and Mg K-edge spectra of MgO, BSE calculations result in better agreement with experiment at high transition energy due to the non-local treatment of the exchange interaction. Recent implementations of BSE in all-electron codes [21, 22] with explicit treatment of core states have demonstrated very good agreement with experiment for the XAS spectra of TiO₂ (rutile and anatase), PbI₂, and CaO [22]. The latter approach is adopted in this work.

Here we describe both the optical and x-ray absorption spectra of bulk MgO including many-body effects. As a first step, we perform the G_0W_0 corrections starting from Kohn-Sham (KS) wavefunctions. We show that careful consideration of the electron-hole interaction with BSE is essential to achieve agreement with experiment for both valence and core excitation spectra. In particular, the optical spectrum calculated with two different DFT functionals (PBEsol and HSE06) including the G_0W_0 and BSE corrections are consistent with experiment [8, 23] and previous theoretical work [17, 18] and yield an im-

proved agreement regarding the intensity of the peaks at higher energies, highlighting the importance of quasiparticle and excitonic effects.

Previous studies have shown that a dense \mathbf{k} -mesh is required for the sampling of the Brillouin zone to describe sufficiently the localization of the excitonic wave function and the fine structure in the vicinity of the absorption edge [11]. Here, we use a model for the static screening with parameters fitted to the G_0W_0 calculation, to solve the BSE (model BSE [11, 24]) starting directly from DFT wavefunctions on a denser \mathbf{k} -mesh, which improves in particular the low energy range (7–11 eV). Beyond previous work we provide a thorough analysis of interband transitions contributing to the peaks in the optical spectrum. Further insight into the nature of the first bound exciton is given by the real-space visualization of its wavefunction.

Employing the `exciting` code, the O and Mg K-edge XAS spectra calculated with BSE show very good agreement with the experimental spectra [25] and with previous theoretical results using the FSR [20]. Knowledge of the origin of peaks is essential for the interpretation of x-ray spectra. The main incentive of this study is to identify the nature of transitions which contribute to the peaks and analyze the character of the first exciton in the O K-edge both in real and reciprocal space.

The paper is structured as follows: the details of the calculations are presented in Section II, followed by the discussion of the results in Section III. We start with the electronic properties of MgO in III A and then compare the optical spectra calculated with two different starting exchange-correlation functionals in III B. Subsequently, we analyze the transitions in reciprocal space to derive the origin of contributions to the peaks in the spectrum. In subsection III C, we present the XAS spectra of the O and Mg K-edge and identify the underlying transitions in reciprocal space for the prominent peaks. Finally, subsection III D is dedicated to the real-space visualization of the first exciton of the optical and the O K-edge x-ray absorption spectrum. The results are summarized in Section IV, followed by two appendices showing a comparison of the optical spectra obtained with VASP and `exciting` and the optical spectrum with the model BSE.

II. COMPUTATIONAL DETAILS

The DFT calculations are performed with the VASP code (version 5.4.4) [26, 27], using pseudopotentials in combination with the projector augmented wave (PAW) method [28], and the `exciting` code [29] (version Nitrogen) employing the all-electron full-potential (linearized) augmented planewave + local orbital [(L)APW+lo] method. For the exchange-correlation functional we chose the generalized gradient approximation (GGA) in the implementation of Perdew, Burke, and Ernzerhof (PBE96) [30], PBEsol [31, 32], and the hybrid functional, HSE06 [33, 34]. The equilibrium lattice constant deter-

mined with the different functionals amounts to 4.24 Å (PBE96), 4.21 Å (PBEsol), and 4.20 Å (HSE06), the experimental one being 4.212 Å [35].

For the calculation of the optical spectrum with VASP, we have performed single-shot G_0W_0 on top of the KS wavefunctions obtained with two DFT functionals, PBEsol and HSE06 and subsequently included excitonic corrections by solving the BSE. For all the BSE calculations the Tamm-Dancoff-approximation (TDA) [36] is adopted. The calculations are performed for a two-atom unit cell with a Γ -centered $15 \times 15 \times 15$ \mathbf{k} -mesh (unless otherwise specified) with a plane-wave cut-off energy of 650 eV. GW PAW pseudopotentials for excited properties were employed in all the calculations with two valence electrons for Mg: $3s^2$ and six for O: $2s^2, 2p^4$. 192 unoccupied bands are used for both the DFT and single-shot G_0W_0 calculations with 100 frequency-grid points. For the optical spectrum a Lorentzian broadening of 0.3 eV is used.

Single-shot G_0W_0 calculations are also performed with the `exciting` code [29] together with BSE [37] for the optical and x-ray absorption spectra [22]. A Γ -centered $11 \times 11 \times 11$ mesh shifted by (0.09, 0.02, 0.04) is employed for the calculations. Muffin-tin radii of 1.058 and 0.767 Å for Mg and O, respectively, are used with a basis set cut-off $R_{MT}|\mathbf{G} + \mathbf{k}|_{max} = 7$, and the lattice constant is set to the PBEsol value of 4.21 Å. The energy threshold to include the local field effects in the excited properties, $|\mathbf{G} + \mathbf{q}|_{max}$, is set to 4.5 a.u.⁻¹ for the optical and O K-edge and 1.5 a.u.⁻¹ for the Mg K-edge absorption spectra. The exchange-correlation functional PBEsol [31, 32] is employed for the Kohn-Sham (KS) states and a total of 192 unoccupied bands are considered in the ground state and G_0W_0 calculation for the optical and O and Mg K-edge x-ray absorption spectra. In the BSE calculation, for the optical spectrum four occupied and five unoccupied bands are considered, while eight unoccupied bands were taken into account for the XAS spectra. A Lorentzian broadening with a width of 0.55 eV is applied to the spectra to mimic the excitation lifetime. The atomic structures and isosurfaces are visualized with the VESTA software [38] and the band structure is calculated with the Wannier90 [39] package in VASP.

III. RESULTS

A. Electronic properties

We start our analysis by comparing the electronic properties obtained from DFT calculations with three different functionals, namely PBE96, PBEsol and HSE06. Table I presents the band gap calculated with VASP. With PBE96 (4.49 eV) and PBEsol (4.58 eV), the band gaps are considerably underestimated, consistent with previous calculations [10–12]. On the other hand, HSE06 renders a band gap of 6.58 eV closest but still below the experimental value of 7.7 and 7.83 eV [8, 9]. The

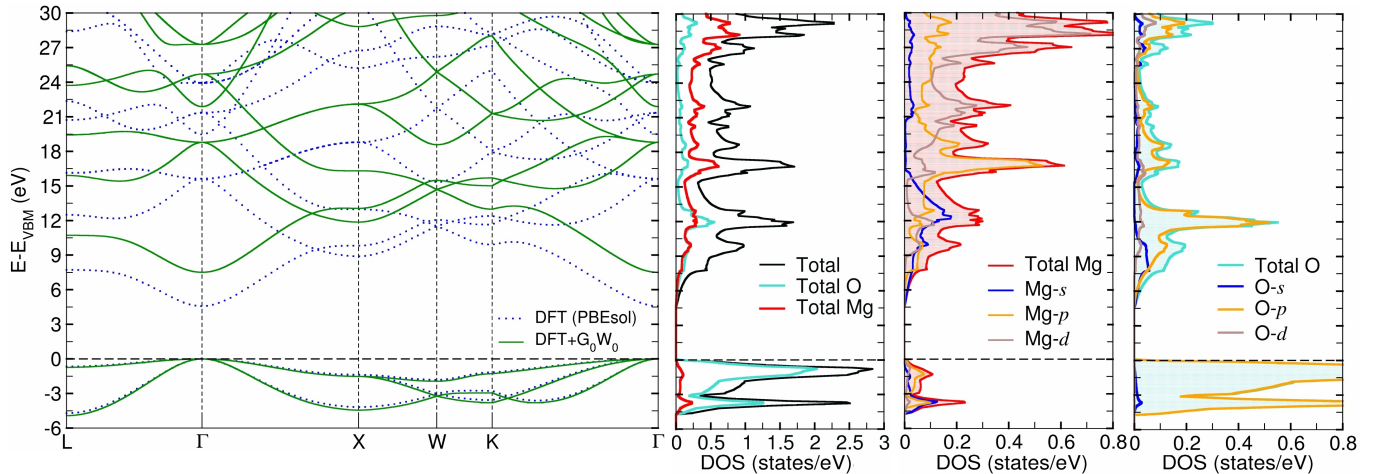


FIG. 1. (a) Kohn-Sham and G_0W_0 band structure and (b-d) total and projected density of states (PDOS) of MgO calculated with PBEsol within VASP.

G_0W_0 band gap obtained with PBEsol (7.52 eV) is closest to experiment, whereas a somewhat lower value (7.26 eV) is obtained with PBE96 which is in agreement with Ref. [12]. In contrast, with HSE06 (8.53 eV) the G_0W_0 band gap is overcorrected. The trend highlights the starting point dependence of the G_0W_0 band gap [40, 41].

Since PBEsol and HSE06 provide better electronic properties as compared to PBE96 we continue the analysis with those. In Fig. 1a the Kohn-Sham and G_0W_0 band structure with the PBEsol functional is plotted along high-symmetry points, showing a direct ($\Gamma - \Gamma$) band gap. The inclusion of quasiparticle effects in the G_0W_0 calculation leads to a nearly rigid shift of the unoccupied Kohn-Sham bands to higher energies. The top of the valence band (VB) consists mainly of O $2p$ states (cf. the projected density of states in Figs. 1b-d) with low dispersion along the $L - \Gamma - K$ direction, whereas the lower bands are more dispersive. Further insight into the orbital-resolved contributions of O and Mg on the band structure is provided in Fig. 2. The bottom of the conduction band (CB) comprises hybridized O $3s$, $3p$, and Mg $3s$ states that are highly dispersive along the $L - \Gamma - X$ and $K - \Gamma$ directions (cf. Figs. 1c, d and Figs. 2a, b, and d). In the range of 4.5 - 11 eV beyond the CB minimum, $3s$, $3p$, and Mg $3s$ states prevail, whereas above 11 eV O $3p$ states become predominant, followed by Mg $3p$ and $3d$ states above 15 eV (cf. Fig. 1d and Figs. 2e, f). We will further analyze the ion- and orbital projections in the band structure in Section III B 3 and Section III C to correlate the contributions with the optical and XAS spectra.

B. Optical properties

Starting from the electronic structure presented in the last section, we determine the optical spectrum including also many-body effects. We discuss the effect of approx-

TABLE I. Comparison of the band gap from the DFT and the G_0W_0 calculation with different starting functionals.

	E_{xc}	IP	G_0W_0	Experiment
E_g (eV) ($\Gamma - \Gamma$)	PBE96	4.49	7.26	7.7 ^a , 7.83 ^b
	PBEsol	4.58	7.52	
	HSE06	6.58	8.53	

^a Reference 8

^b Reference 9

imations to the exchange-correlation functional, namely PBEsol and HSE06, on the spectra and the role of inclusion of G_0W_0 and excitonic corrections with BSE. In addition, the interband transitions responsible for the spectral features are analyzed in reciprocal space.

1. Optical spectrum within IP approximation and inclusion of G_0W_0 corrections

The calculated optical spectra are plotted in Fig. 3 together with the experimental ones [8, 23]. The imaginary part of the experimental dielectric function shows four prominent peaks (marked in Fig. 3b): the first two at ~ 7.7 eV and 10.7 eV are of nearly equal intensity, the third and fourth peak are at 13.32 and 16.9 eV, respectively, with a smaller intensity of the latter. We start our analysis by considering the results from the independent particle (IP) approximation using the KS eigenvalues calculated with the functionals PBEsol and HSE06. The imaginary part of the dielectric function has its onset at 4.58 and 6.58 eV for PBEsol and HSE06, respectively, below the experimental spectrum, due to the underestimation of the band gap (cf. Table I). Moreover, prominent peaks in the imaginary part of the spectrum are observed at ~ 8.5 , 11, and 15.5 eV for PBEsol and at around 11, 13, and 17.5 eV for HSE06, corresponding to pronounced

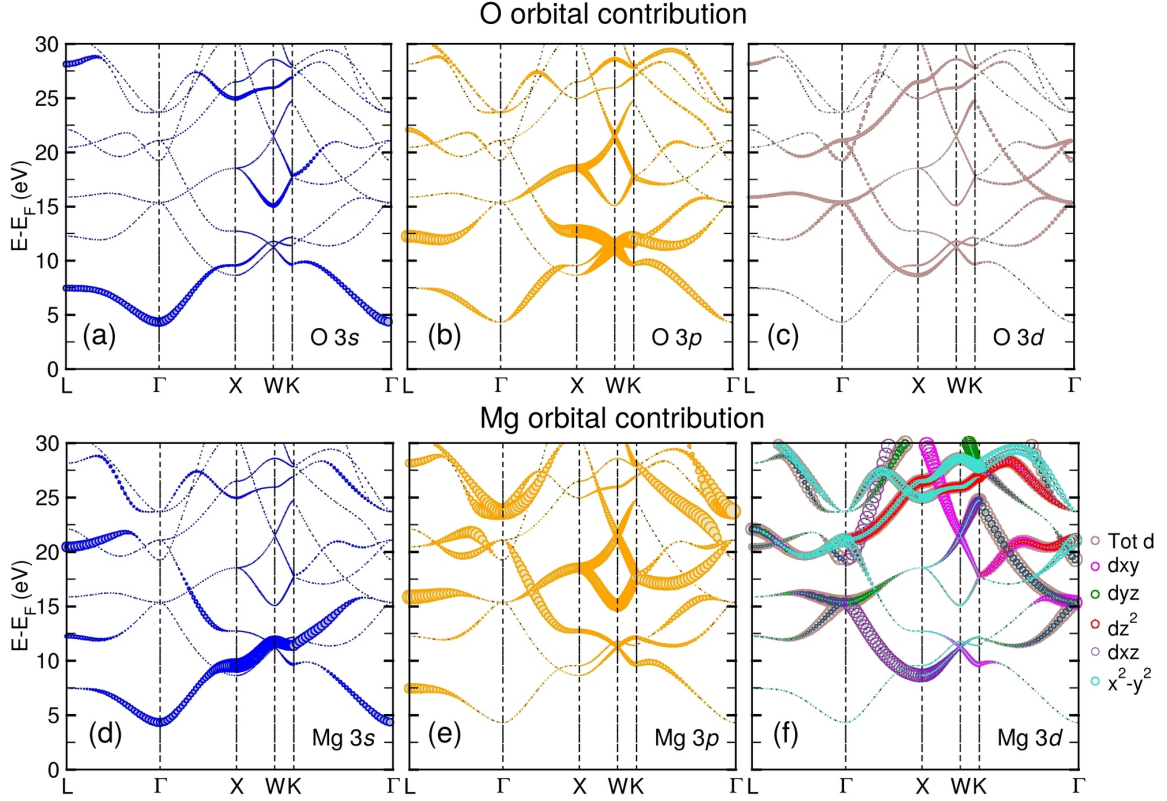


FIG. 2. Oxygen (a-c) and Mg (d-f) orbital-resolved contributions projected on the ground state band structure within VASP.

band transitions that coincide with points of inflection in the real part of the spectrum.

Inclusion of many-body effects within the G_0W_0 approximation results in a blue shift by ~ 3 eV (PBEsol) and 2 eV (HSE06) compared to the IP spectra, due to the increased band gaps within G_0W_0 . This strong effect is attributed to the weak dielectric screening in MgO [13]. In Figs. 3b, d sharper features emerge in ϵ_2 with peaks at ~ 11.8 , 14, and 19 eV (PBEsol), that are shifted to higher energies at ~ 12.5 , 15, and 20.5 eV (HSE06). The real part of the spectrum in Figs. 3a, c exhibits weaker/smoothened features compared to experiment [8] (Fig. 3b, d). The macroscopic static electronic dielectric constant, $\epsilon_\infty = \text{Re } \epsilon(\omega = 0)$ obtained with PBEsol and HSE06 is presented in Table II. Within the IP approximation, ϵ_∞ is overestimated for PBEsol (3.29) compared to the experimental value 2.94 [8], similar to previous results with GGA-PW91 (3.16) [17]. On the other hand, with the hybrid functional, ϵ_∞ is underestimated (2.76). Upon including quasiparticle effects (G_0W_0), the values are substantially reduced to 2.78 (PBEsol) and 2.53 (HSE06).

2. Optical spectrum with excitonic corrections

Additional to the quasiparticle corrections, we consider the effects arising from electron-hole interaction by solv-

TABLE II. Comparison of the macroscopic static electronic dielectric constant ϵ_∞ in the IP approximation and after G_0W_0 and BSE with different DFT functionals.

E_{xc}	IP	G_0W_0	BSE	Experiment
PBEsol	3.29	2.78	3.08	
HSE06	2.76	2.53	2.81	2.94[8]

ing the Bethe-Salpeter equation. The calculations are performed with four occupied and five unoccupied bands which are sufficient to evaluate the optical spectrum up to 30 eV.

The inclusion of excitonic effects leads to a redistribution of the spectral weight to lower energies w.r.t. the G_0W_0 spectrum and the emergence of a sharp peak at the absorption onset. With PBEsol as the starting point in Fig. 3b, the agreement with experiment w.r.t. spectral shape is improved, but the onset of the imaginary part of the dielectric function is ~ 0.7 eV lower than experiment [8, 23]. The prominent peaks are at ~ 7.0 eV, 10 eV, 12.4 eV, and 16 eV. In the real part of the spectrum, the sign reversal at 12.8 eV indicates a plasmonic resonance.

On the other hand, using HSE06 as the starting functional, the real and imaginary part of the spectrum are in excellent agreement with experiment. The peak positions of the distinct features and the plasmonic resonance at 13.4 eV coincide with the experimental ones

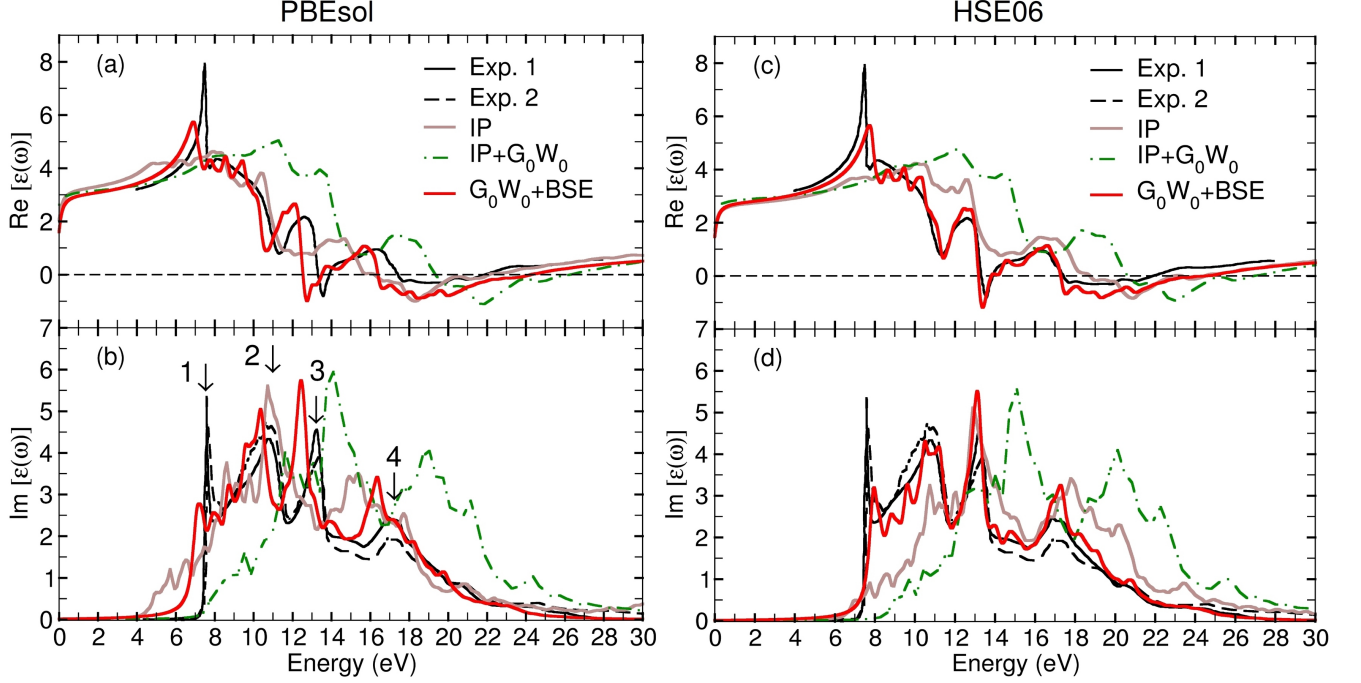


FIG. 3. Optical spectrum of bulk MgO obtained with VASP: (a), (c) real part and (b), (d) imaginary part of the dielectric function for PBEsol and HSE06 as the starting functional, respectively. A Lorentzian broadening of 0.3 eV is employed for all the calculated spectra. The IP, IP+ G_0W_0 , and G_0W_0 +BSE results are shown by brown solid, green dash-dotted, and red solid lines, respectively. Additionally, the experimental data from Exp. 1 [8] (black solid line), and Exp. 2 [23] (black dashed line) are displayed.

[23]. The four peaks of ϵ_2 at $\sim 8, 10.5, 13$, and 17 eV are largely aligned with experiment, as shown in Figs. 3c and d. Further analysis of the origin of the peaks in reciprocal space and the real-space projection of the first exciton are provided in Section III B 3 and Section III D, respectively. The improved description w.r.t. the energetic positions and, to a lesser extent, intensity of the peaks can be attributed to the description of the ground state with a hybrid functional HSE06, the larger number of unoccupied bands considered in the BSE calculation and to performing BSE on top of G_0W_0 . Furthermore, the agreement to experiment concerning the macroscopic static electronic dielectric constant ϵ_∞ is improved after BSE to 3.08 (PBEsol) and 2.81 (HSE06), respectively (cf. Table II), also consistent with a previous value of 3.12 [17], where excitonic corrections were included using the KS eigenenergies and a scissor shift approach. We note that increasing the number of unoccupied bands to 9, leads to slightly higher values for ϵ_∞ 3.16 (PBEsol) and 2.90 (HSE06), the latter being in excellent agreement with experiment. In particular, more empty states are necessary for the calculation of the real part of the dielectric function from the Kramers-Kronig relation. Due to the high computational cost and an enhanced memory demand with more unoccupied bands, we proceed with five unoccupied bands for the further analysis.

Furthermore, for the binding energy of the first exciton we obtain 442 meV with PBEsol and 596 meV with

HSE06. A similar value of 429 meV was obtained by Fuchs *et al.* [11] employing the KS eigenenergies (GGA) with a scissor shift of 2.98 eV and subsequently including excitonic corrections. The overestimation of the binding energy w.r.t experiment (80 meV [8]) may be attributed to the fact that the ionic contributions to the static screening is not considered [42, 43].

3. Analysis of spectral features in reciprocal space

In order to identify the origin of the most prominent peaks, we have performed calculations with the all-electron `exciting` code. The real and imaginary part of the dielectric function for the G_0W_0 +BSE with PBEsol as the DFT functional and similar parameters (four occupied and five unoccupied bands) are plotted in Figs. 4a, b, and show good agreement with experiment as well as the VASP result w.r.t. the energetic positions of the peaks (a comparison of the spectra obtained with the two codes is provided in Appendix A and Fig. 8). The most prominent peaks are marked in Fig. 4b and the corresponding e-h contributions are studied in Figs. 4c-f. We recall that the Bethe-Salpeter equation represents an eigenvalue problem for an effective two-particle Hamiltonian [37, 44]:

$$\sum_{v'c'\mathbf{k}'} H_{v\mathbf{k},v'c'\mathbf{k}'} A_{v'c'\mathbf{k}'}^\lambda = E^\lambda A_{v\mathbf{k}}^\lambda. \quad (1)$$

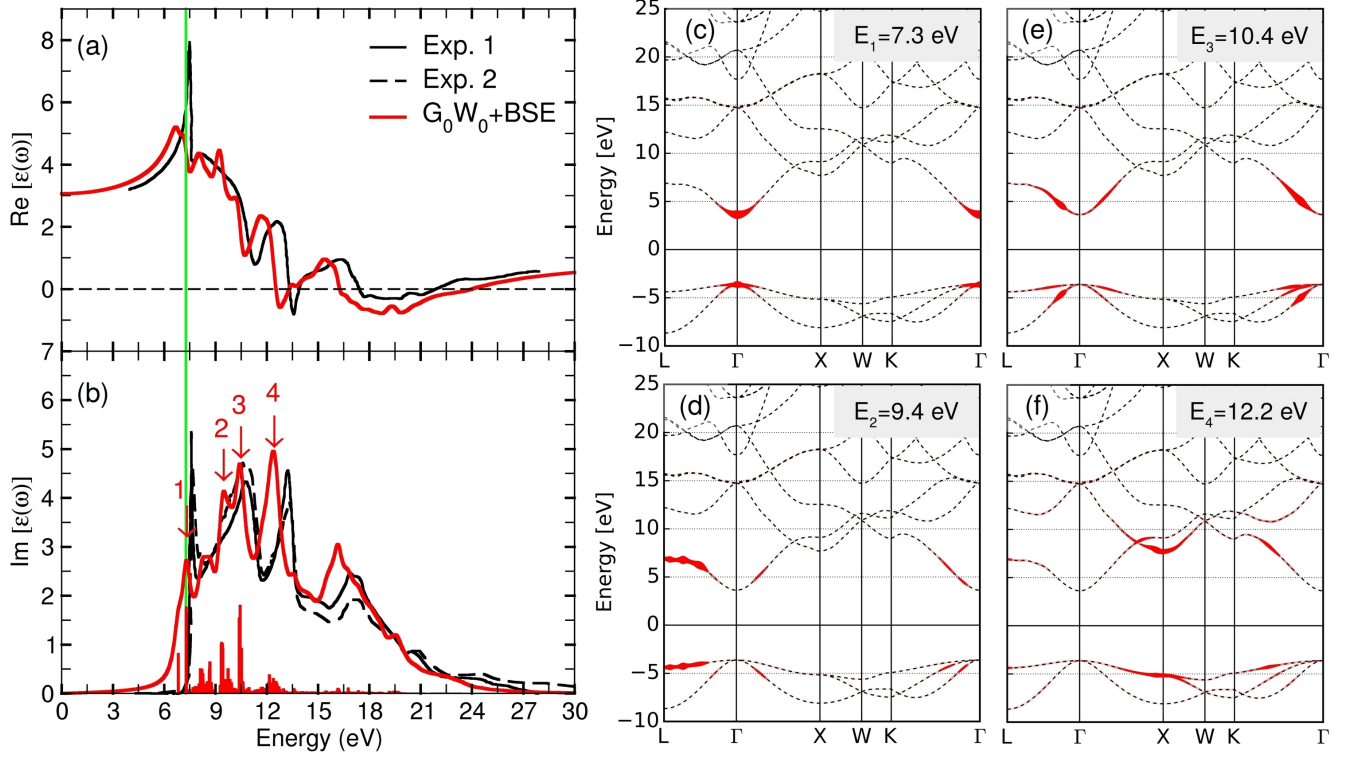


FIG. 4. Optical spectrum with PBEsol including many-body corrections calculated with the `exciting` code: (a) real and (b) imaginary part of the dielectric function. A Lorentzian broadening 0.3 eV is employed for the calculated spectrum for the G_0W_0 +BSE corrections (red line). The direct band gap at 7.26 eV is marked by a vertical green line. Experimental spectra from Roelssler *et al.* [8] (black solid line) and Bortz *et al.* [23] (black dashed line) are shown for comparison. (c–f) electron-hole coupling coefficients represented as circles in reciprocal space for the peaks at different energies marked in (b), where the size of the circle is proportional to the magnitude of the e-h contribution.

where E^λ are the transition energies and $A_{v\mathbf{k}}^\lambda$ are the corresponding states in terms of $v\mathbf{k} \rightarrow c\mathbf{k}$ transitions. The e-h coupling coefficients for a particular transition displayed as circles in Figs. 4c–f are calculated from the BSE eigenvector A^λ as:

$$w_{c\mathbf{k}}^\lambda = \sum_c |A_{v\mathbf{k}}^\lambda|^2, \quad w_{v\mathbf{k}}^\lambda = \sum_v |A_{v\mathbf{k}}^\lambda|^2. \quad (2)$$

The first exciton at 6.82 eV has a binding energy of 435 meV, close to the value obtained with VASP, as discussed in the previous section. This bound exciton contributes to the shoulder at the onset of the spectrum. The interband transitions responsible for the exciton and its real-space distribution are discussed in detail in Section III D.

The first peak at 7.3 eV (cf. Fig. 4c) arises due to transitions from the top of the valence band (VB) to the bottom of the conduction band (CB) around the Γ -point in reciprocal space. A comparison with the site and orbital-projected DOS (Fig. 1) and band structure (Fig. 2) reveals a mixed O 3s, 3p, and Mg 3s character. The second peak at 9.4 eV involves interband transitions from the topmost VB to the lowest CB along $L - \Gamma - X$ and $\Gamma - K$. The CB is more dispersive along $L - \Gamma$ and has mixed O 3s and 3p character with Mg 3p contributions

near L . The next peak at 10.4 eV stems from transitions to the CB from deeper-lying valence bands along $L - \Gamma - X$ and $\Gamma - K$. The final peak at 12.2 eV, plotted in Fig. 4f, results from transitions from the top of the VB to the higher-lying CB around X as well as along $K - \Gamma$. In this energy range, the CB consists of O 3p and Mg 3s and $3d_{xy}, d_{xz}$ states along $\Gamma - X$ and $K - \Gamma$.

C. X-ray absorption spectra

We now turn to the x-ray absorption spectra of the O and Mg K-edge of bulk MgO calculated with the `exciting` code.

1. O K-edge

The theoretical XAS spectrum of the O K-edge is plotted in Fig. 5d together with the experimental spectrum from Luches *et al.* [25], who performed x-ray absorption measurements on MgO films of varying thickness grown epitaxially on Ag(001) as well as on polycrystalline bulk samples. The G_0W_0 +BSE spectrum is characterized by six prominent peaks with high oscillator strength

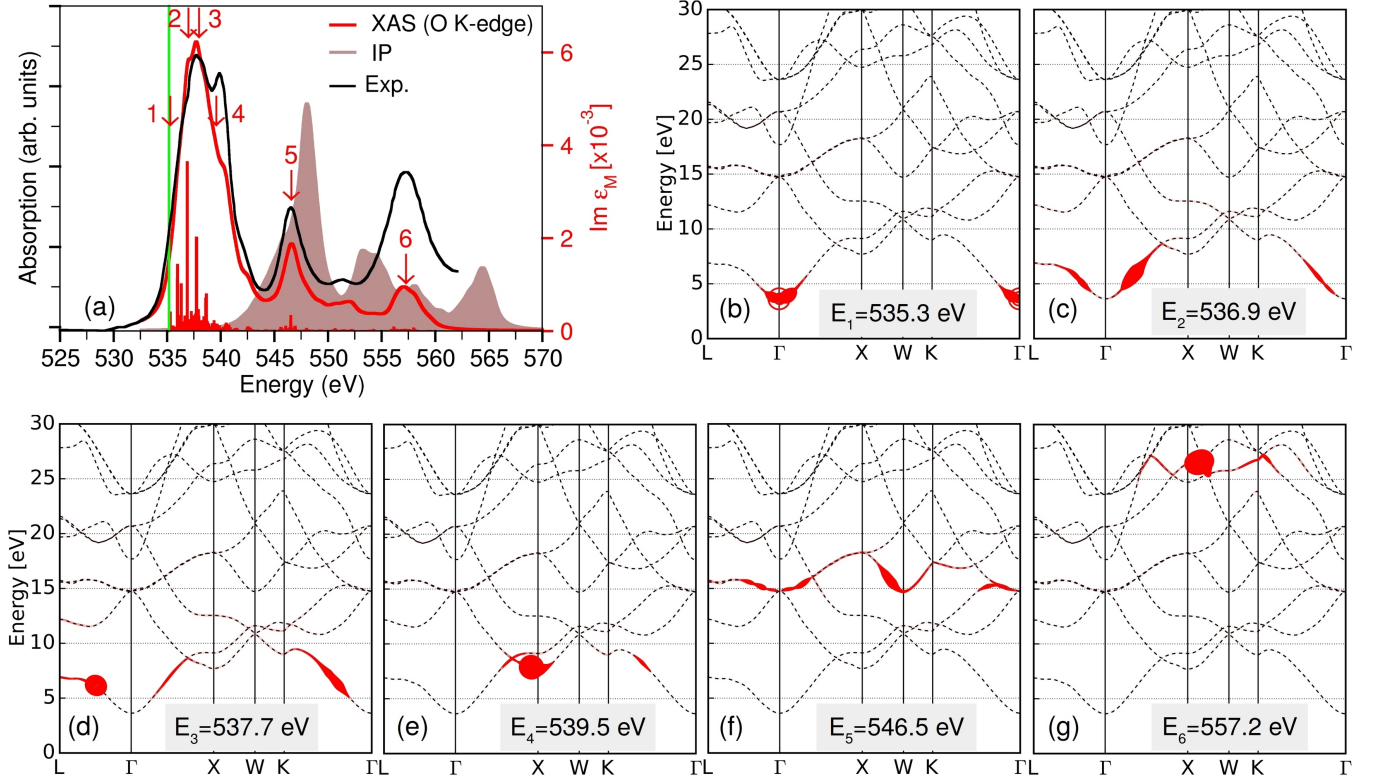


FIG. 5. XAS spectrum of the O K-edge using G_0W_0 +BSE calculated with the **exciting** code: (a) calculated absorption spectra with G_0W_0 +BSE (red line) and IP (brown shaded area) are compared with experimental spectra from Luches *et al.* [25] (black line). A shift of 34.4 eV was applied to the calculated spectra to align to the first peak of the experiment and a Lorentzian broadening of 0.55 eV is adopted to mimic the excitation lifetime. The direct band gap at 535.2 eV is marked by a vertical green line. (b-g) excitonic contributions to the final states in the CB of the peaks marked in (a).

(cf. Fig. 5a). Their origin in terms of transitions to the conduction bands is visualized in Fig. 5b-g.

While the IP spectrum captures the overall shape with four peaks, a very good agreement to experiment concerning the relative positions of the three prominent peaks at ~ 537 , 546, and 557 eV is obtained only after the G_0W_0 +BSE corrections. The spectrum is also consistent with earlier work of Rehr *et al.* [20] using FSR and BSE. The reduced intensity of the third peak in the G_0W_0 +BSE spectrum can be attributed to the limited number of unoccupied bands considered in the calculation.

The first bound exciton is found at 534.5 eV with a binding energy of 691 meV, its real-space distribution is discussed in Section III D. Analysis of the transitions at the onset of the spectrum at 535.3 eV shows that these are localized around Γ at the bottom of the CB (Fig. 5b) and comprise predominantly O $3p$ character hybridized with O $3s$ (cf. Figs. 2a-c), and Mg $3s$ character (cf. Fig. 2d). The second peak at 536.9 eV also arises from transitions to the lowest CB, but is more dispersive along $L - \Gamma - X$ and $K - \Gamma$. The subsequent peak at 537.7 eV stems from transitions to the lowest CB, but is localized midway along the $L - \Gamma$ with some contribution along $K - \Gamma$ and has hybridized O $3s$, $3p$, and Mg $3s$ character.

Furthermore, the peak at 539.5 eV results from transitions to the second lowest unoccupied band localized at X and dispersive along $K - \Gamma$ with Mg $3d_{xz}$ (cf. Fig. 2f) as well as O $3p$ character. Transitions to higher unoccupied bands around W and Γ with mixed O $3p$ and $3d$ and Mg $3p$, t_{2g} character result in a peak at 546.5 eV. The final peak at 557.2 eV arises from transitions to CB at energies above 25 eV with O $3p$ and Mg $3p$, e_g contributions along $X - W - K - \Gamma$.

2. Mg K-edge

Fig. 6a displays the Mg K-edge from the G_0W_0 +BSE calculation and the experimental spectrum from Luches *et al.* [25]. The experimental spectrum has four prominent peaks at 1308.3, 1314.4, and 1316.2 eV, followed by a broader peak at 1326.6 eV, with a noticeable difference in peak intensities for normal and grazing incidence of the MgO film on Ag(001) and for the polycrystalline sample. While the IP spectrum for the O K-edge shows overall agreement with the G_0W_0 +BSE result, for the Mg K-edge the IP spectrum fails to describe the general features of the experimental spectrum. On the other hand, including the core-hole - electron interaction leads

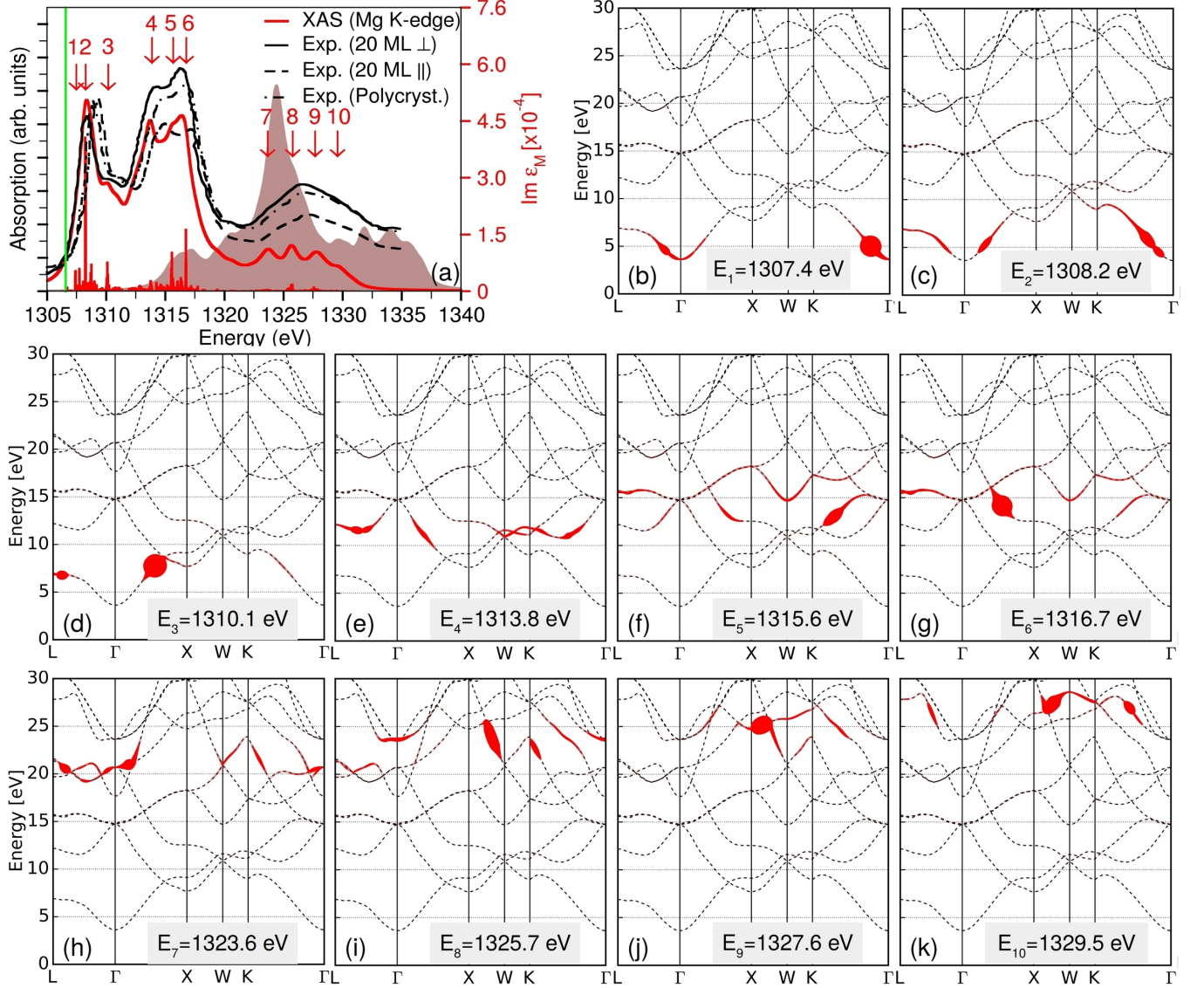


FIG. 6. XAS spectrum of Mg K-edge including G_0W_0 +BSE corrections calculated with the **exciting** code: (a) calculated absorption spectra with G_0W_0 +BS (red line) and IP (brown shaded area) are compared with experimental spectra from Luches *et al.* [25] on a MgO film on Ag(001), grazing/normal incidence of photon beam (black dashed-dotted/solid line); polycrystalline MgO (black dashed line). A shift of 58.8 eV was applied to the calculated spectra to achieve coincidence with the first peak of the experiment and a Lorentzian broadening of 0.55 eV is adopted for the theoretical curve to mimic the excitation lifetime. The direct band gap at 1306.6 eV is marked by a vertical green line. (b-k) excitonic contributions to the final states in the CB of the peaks marked in (a).

to a large redistribution of the spectral weight, accompanied by the emergence of a high intensity peak at the onset of the BSE spectrum. Overall, the G_0W_0 +BSE Mg K-edge is in very good agreement with the experimental spectrum of [25] and with previous BSE and FSR calculations [20] concerning peak positions and relative intensity.

Ten prominent peaks with high oscillator strength are marked which are analyzed further in Figs. 6b-k. The first peak at 1307.4 eV arises from transitions to the bottom of CB with Mg 3p character, hybridized with Mg 3s

states (cf. Figs. 2a,b). The second peak at 1308.2 eV comprises transitions along the $L - \Gamma - X$ with Mg 3p character and along $K - \Gamma$ with mixed Mg 3s and 3p character. The third peak at 1310.1 eV includes transitions to the lowest CB concentrated halfway between $\Gamma - X$ with hybridized Mg 3s and O 3s and 3p character (cf. Figs. 2a,b). Moreover, the peaks at 1313.8, 1315.6, and 1316.7 eV arise from transitions to higher energy CB (>10 eV) and are dispersive along the whole k-path with hybridized O 3p and Mg 3s and 3p as well as Mg $3d_{xz}$ character (cf. Figs. 2d-f). The peaks at 1323.6, 1325.7,

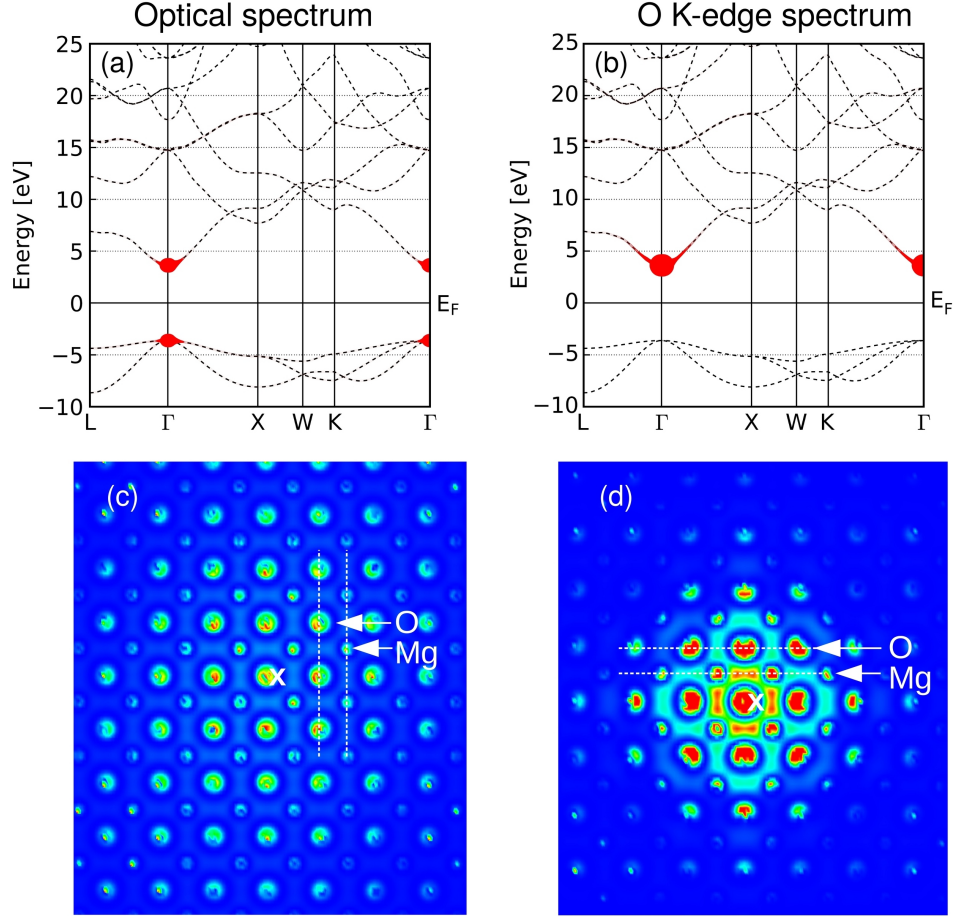


FIG. 7. Analysis of the first exciton in the optical spectrum (a) and O K-edge XAS (b) in reciprocal space. The lower panels show the density associated with the electronic part of the excitonic wavefunctions for a selected cross section in real space: In (c) along $(56\bar{1})$ for the optical excitation shown in (a) and (d) along $(51\bar{6})$ for the O K-edge XAS in (b). The color code visualizes the spacial extension of the wave functions: Blue colors refer to vanishing or low densities, orange to red colors to elevated densities. The hole is fixed near the oxygen (fractional coordinate: 0.52, 0.52, 0.52) and is marked by a white cross.

1327.6, and 1329.5 eV stem from the transitions to the unoccupied bands with $E > 20$ eV predominantly along $X - W - K$ with prevailing hybridized Mg 3p and e_g character.

D. Real-space projection of the first exciton

The real-space wavefunction of the excited electron for a given exciton can be obtained from the BSE eigenvectors A^λ as:

$$\Psi_\lambda(\mathbf{r}_h, \mathbf{r}_e) = \sum_{v\mathbf{k}} A_{v\mathbf{k}}^\lambda \psi_{v\mathbf{k}}^*(\mathbf{r}_h) \psi_{c\mathbf{k}}(\mathbf{r}_e). \quad (3)$$

For more details see Ref. [37, 45] and references therein. For the analysis we fixed the hole slightly off the oxygen position (0.52, 0.52, 0.52) and plotted the electronic part of the wavefunction in real-space for the first exciton of the optical and the O K-edge XAS spectrum in Fig. 7.

The first bound exciton of the optical spectrum (Fig.

7a) consists of transition from the valence band maximum (VBM) to the conduction band minimum (CBM) that are strongly localized around Γ . Since the excited electron is distributed solely over the lowest, highly dispersive conduction band, the bound exciton was previously described in the Wannier-Mott two-band model by Fuchs *et al.* [11]. In Fig. 7c we display a cut along the $(56\bar{1})$ plane through the center of the spread of the wave function near the fixed position of the hole, that shows that the exciton is delocalized over several unit cells which supports the Wannier-Mott character. Moreover the intensity of the spread has a maximum at the oxygen sites and is weaker at the Mg sites. The reciprocal space projection in conjunction with the orbitally projected band structure (cf. Fig. 2) shows a main contribution of hybridized O 3s and Mg 3s states at the CBM.

For comparison, we have also analyzed the real space projection of the first exciton in the O K-edge XAS spectrum. As shown in Fig. 7b this exciton involves tran-

sitions to the CBM, but is more dispersive in reciprocal space along $L - \Gamma - X$ and $K - \Gamma$. This goes hand in hand with a stronger localization in real space, visible from the real space projection in Fig. 7d along the $(\bar{5}\bar{1}\bar{6})$ plane that exhibits a significant decrease in the spread of the wavefunction. Compared to the exciton of the optical spectrum, here the spread is confined to two to three unit cells only. The 2D cut through the center of the wavefunction spread also illustrates the orbital contributions with s and p character near the O sites, whereas the contributions around the Mg sites have s -like character. This can be attributed to the strong hybridization of the O $3s$, $3p$, and Mg $3s$ states around the CBM, discussed above.

IV. SUMMARY

We have provided a comprehensive study of the optical and x-ray absorption spectra of bulk MgO with the VASP and `exciting` codes. The results indicate that the quasiparticle, and in particular excitonic effects are crucial to describe the spectra, concerning peak positions and to a lesser extent intensity.

For the optical spectrum, the effect of two different functionals (GGA-PBESol and the hybrid HSE06) are studied: an excellent agreement with the experiment is obtained with HSE06 w.r.t. the energetic positions of the peaks. Analysis of the electron-hole coupling coefficients in reciprocal space allows us to identify the valence to conduction band transitions contributing to the peaks in the spectrum. In particular, the peak at 7.3 eV arises due to transitions localized around Γ from the top of the VB to the bottom of the CB with mixed O $3s$, $3p$, and Mg $3s$ character, followed by a peak at 9.4 eV stemming from similar interband transitions but along $L - \Gamma - X$ and $\Gamma - K$ with mixed O $3s$, $3p$, and Mg $3p$ character near L . The third peak at 10.4 eV is from transitions to the bottom of CB from deeper lying valence bands and the final peak at 12.2 eV results from a transition to higher lying conduction bands with hybridized O $3p$ and Mg $3s$ and $3d_{xy}, d_{xz}$ character.

The inclusion of core-hole electron interaction by solving the BSE is found to be essential also for the XAS Mg and O K-edge. By visualizing the transitions to the unoccupied bands in reciprocal space, we determine the origin of the relevant peaks in the spectra. In the O K-edge spectrum, the peak at ~ 537 eV originates from the transitions to unoccupied bands with hybridized O $3s$, $3p$, and Mg $3s$ character, the peak at 546 eV stems from O $3p$, $3d$ hybridized with Mg $3p$ and t_{2g} states, and the peak at 557 eV emerges from transitions to the CB with hybridized O $3p$ and Mg $3p$ and $3d$ character. The real space projection of the electronic part of the wavefunction of the first exciton in the optical spectrum shows it has a delocalized Wannier-Mott character, consistent with previous studies in reciprocal space [11]. On the other hand, the wavefunction of the first exciton in

the O K-edge spectrum is stronger localized and spreads up to only three unit cells. We believe that our detailed analysis of the optical and x-ray excitations in this paradigmatic oxide material regarding their orbital character and extension in real and reciprocal space based on state-of-the-art many-body approaches serves as an important benchmark and provides useful background information for the interpretation of experimental data both from static but also time-dependent investigations.

ACKNOWLEDGMENTS

We thank Caterina Cocchi, André Schleife, Heiko Wende, Andrea Eschenlohr, Katharina Ollefs, Nico Rothenbach, and Okan Köksal for fruitful discussions. We wish to acknowledge funding by the Deutsche Forschungsgemeinschaft (DFG, German Research Foundation) within collaborative research center CRC1242 (project number 278162697, subproject C02) and computational time at the Center for Computational Sciences and Simulation of the University of Duisburg-Essen on the supercomputer magnitUDE (DFG grants INST 20876/209-1 FUGG, INST 20876/243-1 FUGG). C. V. and C. D. appreciate funding from Leibniz ScienceCampus GraFOx.

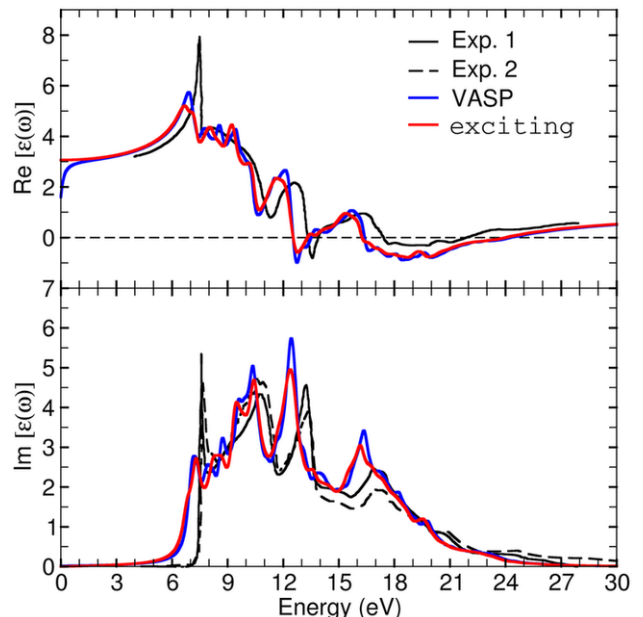


FIG. 8. Comparison of the G_0W_0 +BSE spectrum calculated with PBESol as the starting functional with `exciting` (red solid line) and VASP (blue solid line). The spectra are compared with the experiments of Roelssler *et al.* [8] (black solid line) and Bortz *et al.* [23] (black dashed line). A Lorentzian broadening of 0.3 eV is employed for the theory spectra.

Appendix A: Comparison of the optical spectrum calculated with exciting and VASP

The optical spectra obtained with `exciting` and VASP with the same exchange-correlation functional (PBEsol) in Fig. 8 show very good agreement in the overall shape and peak positions with some smaller differences in peak heights.

Appendix B: DFT+model-BSE (mBSE)

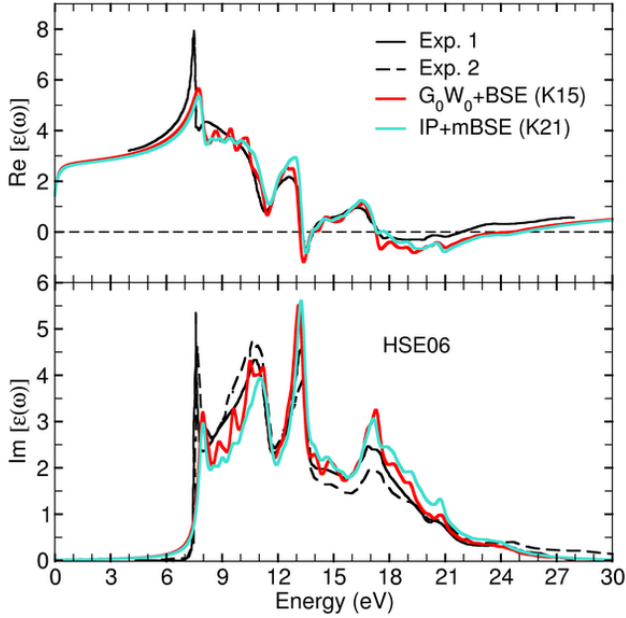


FIG. 9. Comparison of the spectrum obtained with mBSE on top of DFT (k -mesh of $21 \times 21 \times 21$) and with G_0W_0 +BSE corrections (k -mesh of $15 \times 15 \times 15$). The spectra were calculated with HSE06 as the starting functional and compared with the experiments of Roelssler *et al.* [8] (black solid line) and Bortz *et al.* [23] (black dashed line). A Lorentzian broadening of 0.3 eV is employed for the theory spectra.

Fuchs *et al.* [11] have pointed out the importance of using a dense k -mesh for BSE in order to obtain convergence of the optical spectrum in the lower energy range. However, this goes hand in hand with a high computation cost in the G_0W_0 calculation. One way to circumvent this is to perform a model BSE calculation directly using the DFT wave functions and considering only the required number of bands which cover the energy range of interest [11]. The omission of the G_0W_0 step allows us to use a higher k -mesh and thus improve the convergence. Here, we discuss the result obtained by using a model for the static screening with parameters fitted to the screened Coulomb kernel diagonal values obtained from G_0W_0 calculation, a detailed description can be found in Ref. [11, 24, 46, 47] and was previously used in Ref. [24, 46]. Good agreement between mBSE and the

full BSE (G_0W_0 +BSE) was recently obtained for bulk SrTiO₃ [41].

In our study, mBSE is performed on a $21 \times 21 \times 21$ k -mesh with a range separation parameter $\lambda = 1.44 \text{ \AA}^{-1}$, ion-clamped static dielectric function $\epsilon_\infty^{-1} = 0.38974$, and a scissor shift of 1.95 eV, corresponding to the difference between the KS energies obtained with HSE06 and the quasiparticle band gap. In Fig. 9 the spectrum from mBSE and full BSE obtained with HSE06 as the starting functional on a k -mesh of $15 \times 15 \times 15$ are displayed. Overall, very good agreement is obtained. In particular, in the energy range of 7 – 11 eV we even observe a better agreement with experiment for mBSE when compared with full BSE associated with the increase in k -point density. For energies higher than 11 eV, the positions of the peaks are also well reproduced with the mBSE approach with slight increase in the intensity when compared with the full BSE spectrum. The good agreement between the mBSE and full BSE spectra is attributed to the fact that the electronic structure does not change significantly from DFT to G_0W_0 (cf. Fig. 1), the prevailing effect being a rigid shift of the conduction band. The binding energy of the first exciton from mBSE is 610.8 meV.

-
- [1] T. Maruyama, Y. Shiota, T. Nozaki, K. Ohta, N. Toda, M. Mizuguchi, A. A. Tulapurkar, T. Shinjo, M. Shiraishi, S. Mizukami, Y. Ando, and Y. Suzuki, *Nature Nanotech* **4**, 158 (2009).
- [2] R. G. S. Sofin, S. K. Arora, and I. V. Shvets, *Journal of Applied Physics* **97**, 10D315 (2005).
- [3] S. Yang, H. Park, J. Kim, J. Kim, and B. Park, *Journal of Applied Physics* **110**, 093920 (2011).
- [4] A. Melnikov, I. Razdolski, T. O. Wehling, E. T. Papaioannou, V. Roddatis, P. Fumagalli, O. Aktsipetrov, A. I. Lichtenstein, and U. Bovensiepen, *Phys. Rev. Lett.* **107**, 076601 (2011).
- [5] N. Rothenbach, M. E. Gruner, K. Ollefs, C. Schmitz-Antoniak, S. Salamon, P. Zhou, R. Li, M. Mo, S. Park, X. Shen, S. Weathersby, J. Yang, X. J. Wang, R. Pentcheva, H. Wende, U. Bovensiepen, K. Sokolowski-Tinten, and A. Eschenlohr, *Phys. Rev. B* **100**, 174301 (2019).
- [6] M. E. Gruner and R. Pentcheva, *Phys. Rev. B* **99**, 195104 (2019).
- [7] Y. Beyazit, J. Beckord, P. Zhou, J. P. Meyburg, F. Kühne, D. Diesing, M. Ligges, and U. Bovensiepen, *Phys. Rev. Lett.* **125**, 076803 (2020).
- [8] D. M. Roessler and W. Walker, *Phys. Rev.* **159**, 733 (1967).
- [9] R. C. Whited, C. J. Flaten, and W. W. C., *Solid State Communications* **13**, 1903 (1973).
- [10] A. Schleife, F. Fuchs, J. Furthmüller, and F. Bechstedt, *Phys. Rev. B* **73**, 245212 (2006).
- [11] C. Fuchs, A. Rödl, A. Schleife, and F. Bechstedt, *Phys. Rev. B* **78**, 085103 (2008).
- [12] M. Shishkin and G. Kresse, *Phys. Rev. B* **75**, 235102 (2007).
- [13] N.-P. Wang, M. Rohlfing, P. Krüger, and J. Pollmann, *Applied Physics A* **78**, 213 (2004).
- [14] H. L., *Phys. Rev.* **139**, A739 (1950).
- [15] E. D. Palik, *Handbook of Optical Constants of Solids*, Vol. 2 (Academic, Orlando, 1991).
- [16] J. P. Perdew and Y. Wang, *Phys. Rev. B* **45**, 13244 (1992).
- [17] A. Schleife, C. Rödl, F. Fuchs, J. Furthmüller, and F. Bechstedt, *Phys. Rev. B* **80**, 035112 (2009).
- [18] A. Schleife and F. Bechstedt, *Journal of Materials Research* **27**, 2180 (2012).
- [19] U. von Barth and G. Grossmann, *Phys. Rev. B* **25**, 5150 (1982).
- [20] J. J. Rehr, J. A. Soininen, and E. L. Shirley, *Physica Scripta* **T115**, 207 (2005).
- [21] R. Laskowski and P. Blaha, *Phys. Rev. B* **82**, 205104 (2010).
- [22] C. Vorwerk, C. Cocchi, and C. Draxl, *Phys. Rev. B* **95**, 155121 (2017).
- [23] M. L. Bortz, R. H. French, D. J. Jones, R. V. Kasowski, and F. S. Ohuchi, *Physica Scripta* **41**, 537 (1990).
- [24] P. Liu, B. Kim, X.-Q. Chen, D. D. Sarma, G. Kresse, and C. Franchini, *Phys. Rev. Materials* **2**, 075003 (2018).
- [25] P. Luches, S. D’Addato, S. Valeri, E. Groppo, C. Prestipino, C. Lamberti, and F. Boscherini, *Phys. Rev. B* **69**, 045412 (2004).
- [26] G. Kresse and J. Furthmüller, *Comput. Mater. Sci.* **6**, 15 (1996).
- [27] G. Kresse and J. Furthmüller, *Phys. Rev. B* **54**, 11169 (1996).
- [28] G. Kresse and D. Joubert, *Phys. Rev. B* **59**, 1758 (1999).
- [29] A. Gulans, S. Kontur, C. Meisenbichler, D. Nabok, P. Pavone, S. Rigamonti, S. Sagmeister, U. Werner, and C. Draxl, *Journal of Physics: Condensed Matter* **26**, 363202 (2014).
- [30] J. P. Perdew, K. Burke, and M. Ernzerhof, *Phys. Rev. Lett.* **77**, 3865 (1996).
- [31] J. P. Perdew, A. Ruzsinszky, G. I. Csonka, O. A. Vydrov, G. E. Scuseria, L. A. Constantin, X. Zhou, and K. Burke, *Phys. Rev. Lett.* **100**, 136406 (2008).
- [32] J. P. Perdew, A. Ruzsinszky, G. I. Csonka, O. A. Vydrov, G. E. Scuseria, L. A. Constantin, X. Zhou, and K. Burke, *Phys. Rev. Lett.* **102**, 039902 (2009).
- [33] J. Heyd, G. E. Scuseria, and M. Ernzerhof, *J. Chem. Phys.* **118**, 8207 (2003).
- [34] J. Heyd, J. E. Peralta, G. E. Scuseria, and R. L. Martin, *J. Chem. Phys.* **123**, 174101 (2005).
- [35] Landolt-Börnstein, *Numerical Data and Functional Relationships*, Vol. 7, Part b (Springer, Berlin, 1975).
- [36] S. M. Dancoff, *Phys. Rev.* **78**, 382 (1950).
- [37] S. Sagmeister and C. Ambrosch-Draxl, *Phys. Chem. Chem. Phys.* **11**, 4451 (2009).
- [38] K. Momma and F. Izumi, *J. Appl. Crystallogr.* **44**, 1272 (2011).
- [39] A. A. Mostofi, J. R. Yates, Y.-S. Lee, I. Souza, D. Vanderbilt, and N. Marzari, *Computer Physics Communications* **178**, 685 (2008).
- [40] H. Jiang, R. I. Gomez-Abal, P. Rinke, and M. Scheffler, *Phys. Rev. Lett.* **102**, 126403 (2009).
- [41] V. Begum, M. Gruner, and R. Pentcheva, *Physical Review Materials* **3**, 065004 (2019).
- [42] K. Shindo, *Journal of the Physical Society of Japan* **29**, 287 (1970).
- [43] R. Zimmermann, *physica status solidi (b)* **48**, 603 (1971).
- [44] M. Rohlfing and S. G. Louie, *Phys. Rev. B* **62**, 4927 (2000).
- [45] C. Vorwerk, B. Aurich, C. Cocchi, and C. Draxl, *Electronic Structure* **1**, 037001 (2019).
- [46] M. Bokdam, T. Sander, A. Stroppa, S. Picozzi, D. D. Sarma, C. Franchini, and G. Kresse, *Sci. Rep.* **6**, 28618 (2015).
- [47] F. Bechstedt, R. Del Sole, G. Cappellini, and L. Reining, *Solid State Communications* **84**, 765 (1992).